J. Fluid Mech. (1972), *vol.* 53, *part* 4, *pp.* 611–636
Printed in Great Britain

On the structure of hypersonic turbulent boundary layers

By F. K. OWEN AND C. C. HORSTMAN
Ames Research Center, NASA, Moffett Field, California

(Received 28 September 1971 and in revised form 7 February 1972)

Extensive hot-wire auto- and cross-correlation measurements obtained in a fully developed compressible turbulent boundary layer are presented. A tentative mechanism of turbulence production and growth in hypersonic flow suggested by these measurements is developed. This flow model is consistent with previous observations in incompressible flows. Detailed measurements of the mean properties of the hypersonic turbulent boundary layer are also presented and compared with results from various transformation and finite-difference prediction methods. It is shown that none of the theories predict all the properties of the hypersonic turbulent boundary layer and that additional measurements are needed to provide more adequate physics of turbulent processes for use in the various theories.

1. Introduction

In recent years extensive experimental and analytical work has been conducted on supersonic and hypersonic turbulent boundary layers but very few measurements are of a quality high enough to serve as a guide for the various calculation schemes, and even fewer are of the type that could give more insight into the turbulent motion itself. Consequently very little is known about the structure of hypersonic turbulent boundary layers. Indeed Laufer (1968) has pointed out the general failure of experimenters to exploit the advantages of hot-wire anemometry for fluctuation measurements.

Since turbulent flows vary not only in time but also in space, their investigation must involve an examination of both the spatial and temporal statistical structure. Space–time correlations can make a contribution to this study since they give evidence of the heredity and structure of turbulence, as well as values of the convection velocities of the vorticity and entropy modes compared with the average mass transport velocities. Such measurements have been made in incompressible turbulent boundary layers (e.g. Favre, Gaviglio & Dumas 1967) but, to the authors' knowledge, no such measurements have been reported for compressible turbulent boundary layers.

In the present investigation extensive hot-wire correlation measurements were obtained. These data provide new information on the turbulent structure of a hypersonic boundary layer. Profile data are also presented which fully document the mean properties of a turbulent hypersonic boundary layer of sufficient length which is fully established and has known boundary conditions.

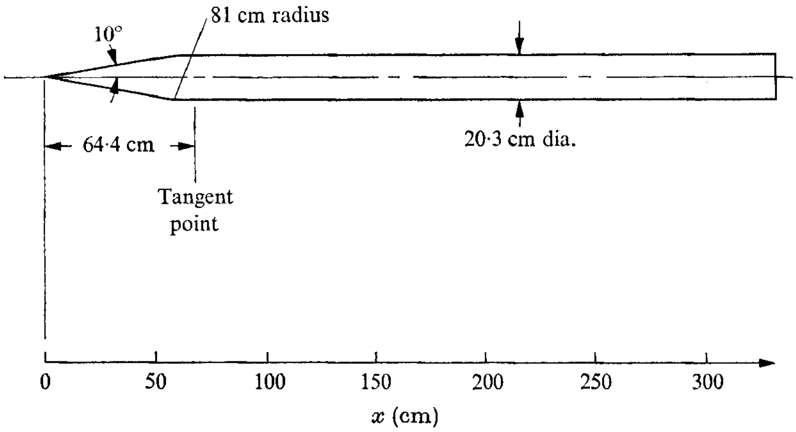

FIGURE 1. Test model.

With the recent development of finite-difference calculation methods for solving the hypersonic boundary layer, the need for a completely documented flow which can be used to evaluate these methods is evident. There have been several experimental studies of hypersonic turbulent boundary layers but these are mostly incomplete in that limited measurements were obtained for each flow. In addition a significant portion of the available studies are for wind tunnel nozzle-wall boundary layers, for which unknown upstream influences have yielded results giving unexplained differences between flat-plate flows and nozzle-wall flows.

2. Experimental procedure

2.1. *Wind tunnel*

The investigation was conducted in air in the Ames 3·5 ft hypersonic wind tunnel. High-pressure air which can be heated up to 1170 °K in a pebble-bed heater flows through the 1·067 m diameter test section to low-pressure spheres. The present test conditions were: total temperature $T_0 = 667$ °K, total pressure $p_0 = 34$ atm, free-stream unit Reynolds number $Re_\infty = 0{\cdot}109 \times 10^6\,\mathrm{cm}^{-1}$, free-stream Mach number $M_\infty = 7{\cdot}2$. The test core diameter is approximately 0·70 m with axial Mach number gradients less than $0{\cdot}12\,\mathrm{m}^{-1}$. Useful test time was two minutes.

2.2. *Test model configuration*

To meet an objective of this investigation a test model which could provide a fully developed turbulent boundary layer over a length of 100 boundary-layer thicknesses after transition was required. Therefore an axisymmetric cone-ogive-cylinder was chosen. Characteristics theory indicated a zero pressure gradient region over most of the cylindrical portion of the model. The test model, shown in figure 1, was 330 cm long and 20·3 cm in diameter.

The surface pressure data are compared with characteristics theory in figure 2. Reasonable agreement between theory and experiment is obtained. The pressures

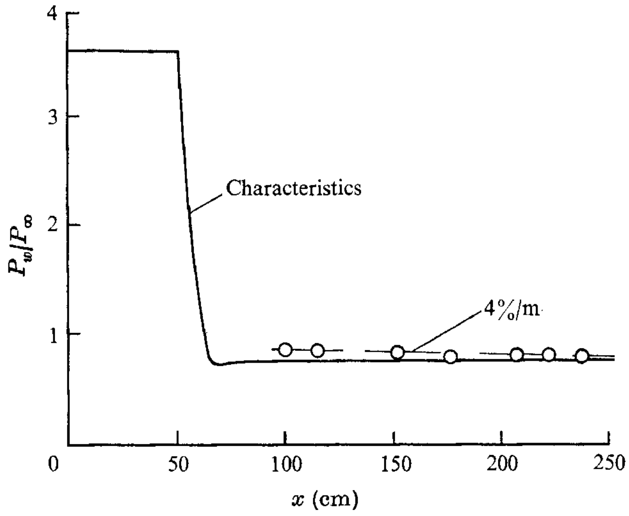

FIGURE 2. Model wall pressure distribution.

are slightly higher than those predicted by theory owing to boundary-layer displacement effects. The pressure gradient is slightly favourable with an average variation of $(1/p)\,dp/dx$ of -4 %/m. To ensure that the test model was aligned with the flow, surface pressure and heat-transfer measurements were obtained at 90° intervals around the model and surface skin-friction measurements 180° apart. Variations in the data around the model were within the experimental accuracy of the measurements.

2.3. *Test model boundary conditions*

Natural transition from laminar to turbulent flow was measured by a hot wire close to the model surface. Using a method based on the thin-film gauge technique for detecting boundary-layer transition (Owen 1970), the beginning and end of transition were determined to be at $x = 37$ and 80 cm respectively. During a 1 min test the model wall temperature increased a maximum of 40 °K on the cone portion of the model and 10 °K on the cylindrical portion. All tests except a few hot-wire surveys required less than 1 min. The average model wall temperature T_w was 310 °K.

To determine boundary-layer edge conditions characteristics theory was used up to $x = 80$ cm. For larger values of x, the edge conditions were interpolated from a faired curve through the measured edge conditions at each survey location and characteristics values at $x = 80$ cm. These values are tabulated in table 1. The boundary-layer edge is defined as the height in the boundary layer where the Pitot pressure reaches 99 % of the local free-stream value.

2.4. *Hot-wire measurements*

The turbulent fluctuations were measured using a constant-temperature hot-wire anemometer system. The frequency response of the system enabled fluctuation scales down to one-fifth of the boundary-layer thickness to be recorded and

x (cm)	U_e/U_∞	M_e/M_∞	ρ_e/ρ_∞	Re_e/Re_∞	δ (cm)
0	0·975	0·795	2·39	1·54	—
20	0·975	0·795	2·39	1·54	—
40	0·975	0·795	2·39	1·54	—
60	0·995	0·945	1·12	0·96	—
80	1·00	1·017	0·79	0·81	—
100	1·00	1·005	0·85	0·85	1·50
120	1·00	1·000	0·83	0·825	1·76
140	1·00	1·000	0·83	0·815	2·02
160	1·00	0·995	0·82	0·805	2·28
180	1·00	0·990	0·81	0·80	2·55
200	1·00	0·985	0·795	0·78	2·82
220	1·00	0·980	0·78	0·76	3·08
240	1·00	0·975	0·765	0·74	3·35

TABLE 1. Boundary-layer edge conditions. $M_\infty = 7{\cdot}2$, $T_{0\infty} = 667$ °K, $T_w = 310$ °K, $U_\infty = 1110\,\mathrm{m\,s^{-1}}$, $Re_\infty = 0{\cdot}109\times10^6\,\mathrm{cm^{-1}}$.

correlated. The a.c. component of the hot-wire signals, representing the turbulent fluctuations, was recorded on the F.M. system of a multichannel tape recorder. For the correlation measurements, the signals from two hot wires were recorded simultaneously on two tape recorder channels which had been previously checked for phase differences. The auto- and cross-correlations were then obtained by playing back the tapes through an analog correlator. The filtered correlations were obtained using matched $\frac{1}{3}$ octave filters. Since all the longitudinal cross-correlation data were obtained at separation distances between 50 and 185 times the wire length no wire length corrections were necessary.

3. Mean flow field measurements

Mean velocity, Mach number and density measurements are presented in figures 3, 4 and 5 respectively. As the streamwise distance from the model apex (x) is increased from 115 to 237 cm these profiles remain approximately similar. Some of the differences between the profiles are probably due to small errors in the determination of the boundary-layer thickness for each x location. The velocity profiles show that the flow is a fully developed turbulent flow approximated by a one-seventh power-law variation which would be expected for the Reynolds number range of these tests. In table 2 the following measured boundary-layer quantities are tabulated: boundary-layer thickness δ, boundary-layer displacement thickness

$$\delta^* = \int_0^\delta \left(1-\frac{\rho U}{\rho_e U_e}\right)\left(1+\frac{y}{r}\right)dy,$$

boundary-layer momentum thickness

$$\theta = \int_0^\delta \left(\frac{\rho U}{\rho_e U_e}\right)\left(1-\frac{U}{U_e}\right)\left(1+\frac{y}{r}\right)dy,$$

shape factor $H = \delta^*/\theta$, velocity exponent N, defined by $U/U_e = (y/\delta)^{1/N}$, local skin friction coefficient C_f, friction velocity $U_\tau = (\tau_w/\rho_w)^{\frac{1}{2}}$, local Stanton number

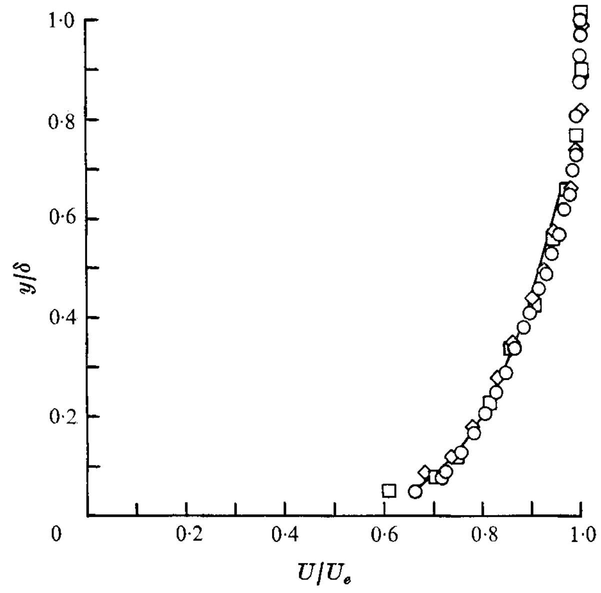

FIGURE 3. Mean velocity profiles across the boundary layer at three stations on the model. ○, $x = 237$ cm; □, $x = 176$ cm; ◇, $x = 115$ cm; —, $U/U_e = (y/\delta)^{\frac{1}{7}}$.

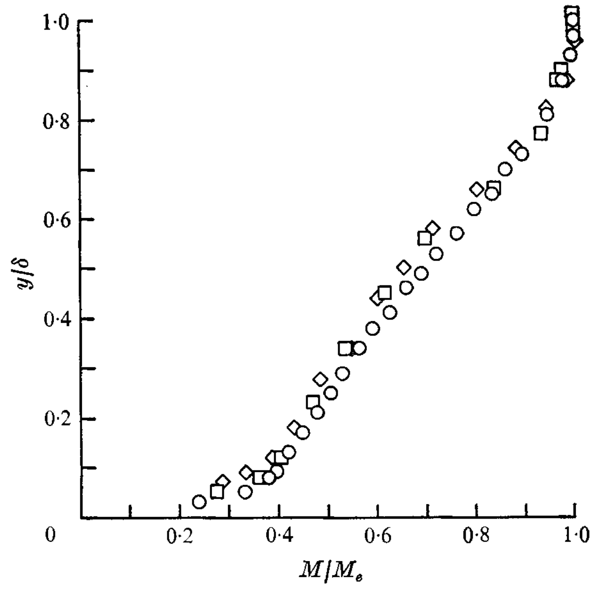

FIGURE 4. Mean Mach number profiles across the boundary layer at three stations on the model. ○, $x = 237$ cm; □, $x = 176$ cm; ◇, $x = 115$ cm.

C_h, and the Reynolds analogy factor $2C_h/C_f$. The values of N and δ^*/δ are nearly constant along the test model. However, the shape factor decreases with increasing x. Finite-difference calculations, to be discussed in the appendix, also predict a decrease.

The mean measurements presented in the appendix provide a thorough docu-

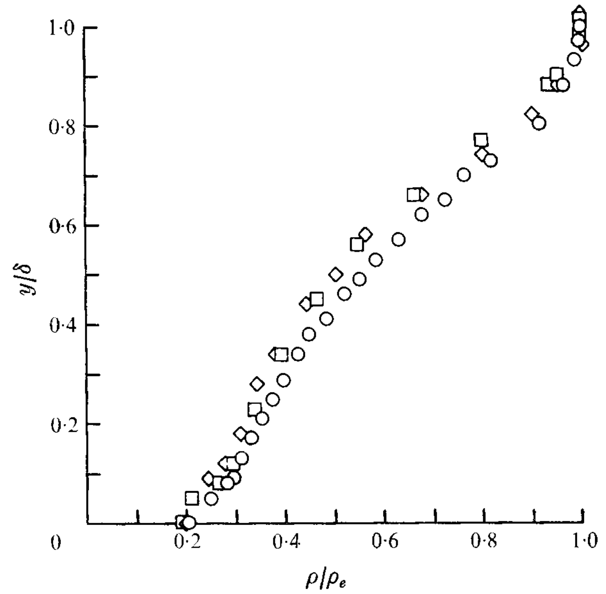

FIGURE 5. Mean density profiles across the boundary layer at three stations on the model. ○, x = 237 cm; □, x = 176 cm; ◇, x = 115 cm.

x (cm)	δ (cm)	δ^* (cm)	θ (cm)	δ^*/δ	$H = \delta^*/\theta$	N	$C_f^* \times 10^3$	U_τ, m s^{-1}	$C_h^* \times 10^3$	$2C_h/C_f$
85	—	—	—	—	—	—	0·925	58·0	0·586	1·27
96	—	—	—	—	—	—	—	—	0·556	—
115	1·7	0·867	0·0535	0·51	16·2	6·32	—	—	0·510	—
146	—	—	—	—	—	—	0·875	52·2	0·466	1·07
166	—	—	—	—	—	—	—	—	0·454	—
176	2·5	1·300	0·0832	0·52	15·6	6·97	0·855	51·5	0·458	1·07
207	—	—	—	—	—	—	—	—	0·486	—
227	—	—	—	—	—	—	—	—	0·472	—
237	3·3	1·617	0·1188	0·49	13·6	6·97	0·801	50·3	0·484	1·21

TABLE 2. Boundary-layer integrals and local surface skin friction and heat transfer. Superscript * indicates average of values of the data at each location.

mentation of a fully developed hypersonic turbulent boundary layer. It is shown that none of the various theories, based on the time-averaged conservation equations, predict all the properties of the hypersonic turbulent boundary layer. The method which seems to offer the most promise is the finite-difference solution to the full partial differential boundary-layer equations. This method can easily be extended to flows with a pressure gradient. However, without some empirical information as to the correct eddy viscosity and turbulent Prandtl number variations across the boundary layer, exact agreement between theory and experiment cannot be obtained. Perhaps detailed measurement of the turbulent structure will eventually provide a better Reynolds stress model and allow a better physical model for the turbulent transport process.

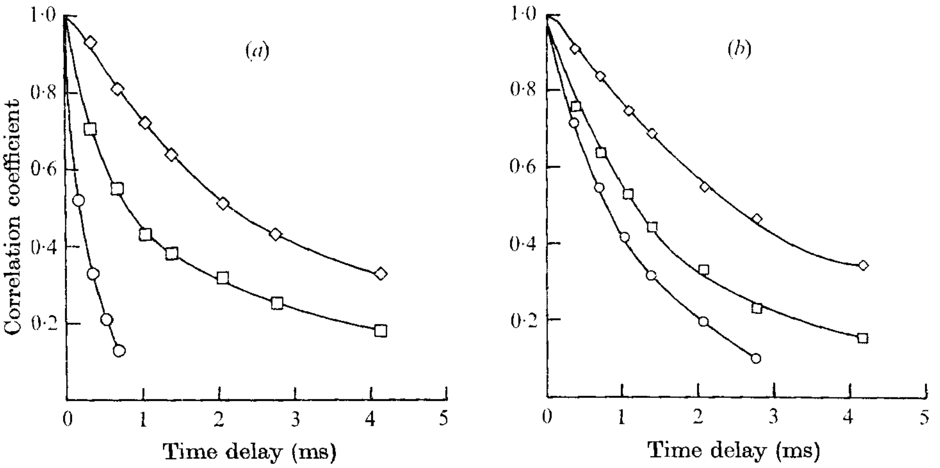

FIGURE 6. Autocorrelation measurements at three positions in the flow. ○, $y/\delta = 0{\cdot}01$; □, $y/\delta = 0{\cdot}3$; ◇, $y/\delta = 2{\cdot}5$. (*a*) $x = 176$ cm. (*b*) $x = 237$ cm.

4. Hot-wire correlation measurements

Cross-correlation measurements involve the correlation of signals from two spatially separated measuring positions, with varying positive or negative time delays of one signal with respect to the other. Thus if $V_1(x_1, y_1, z_1, 0)$ denotes the signal received at one point at time $t = 0$ and $V_2(x_2, y_2, z_2, t)$ denotes the signal received at a second point at time t their cross-correlation coefficient may be defined as

$$R(V_1, V_2) = \frac{\overline{V_1 V_2}}{(\overline{V_1^2})^{\frac{1}{2}}\,(\overline{V_2^2})^{\frac{1}{2}}},$$

where the bars denote time averages. The space correlation, which involves the comparison of the instantaneous signal received at two spatially separated points, is therefore the cross-correlation at zero time delay, while the autocorrelation, which involves the correlation of a signal received at one measuring station with the signal received at the same point at time t, is the cross-correlation for zero separation.

4.1. *Auto- and cross-correlation measurements*

Figure 6 (*a*) shows the autocorrelation of the fluctuating signals at the $x = 176$ cm location at two positions in the boundary layer and in the far field. It can be seen that there is a marked variation of energy distribution with frequency across the boundary layer and that, as will be shown, the far field contains proportionately much less energy in the high wavenumber range than the wall region. At the $x = 237$ cm location (see figure 6 (*b*)) the results are qualitatively the same but with increased energy at lower frequencies, corresponding to the increase of the turbulence scale with increasing boundary-layer thickness. The energy spectra variations across the boundary layer at the forward station obtained by Fourier transformation of the autocorrelation curves are shown in figure 7. Since the smallest turbulence scales measured were three times the wire length no wire

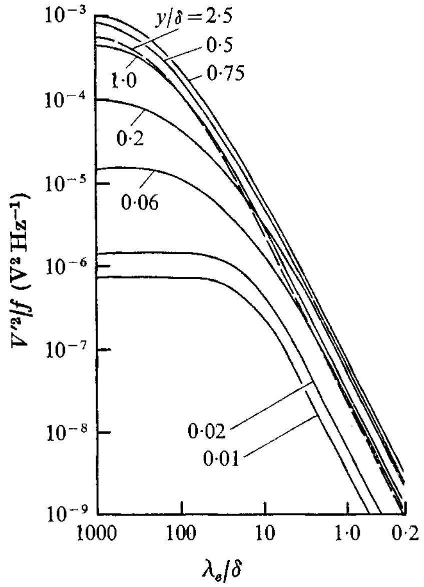

FIGURE 7. Energy spectra distributions as a function of disturbance scale ($\lambda_e = U_e/2\pi f$) across the boundary layer and in the local free stream at $x = 176$ cm.

length corrections have been applied to the turbulence spectra measurements. The maximum fluctuation energy occurs near the boundary-layer edge

$$(y/\delta \approx 0{\cdot}75).$$

As the wall is approached the energy levels decrease, but there is proportionally more energy associated with the smaller scale disturbances. This 'movement' of the relative energy to the smaller scales is believed to be due to the extremely large rates of shear near the wall.

The peaks of the cross-correlations obtained for various values of wire separation distance represent the autocorrelation in a reference frame moving with the disturbances. They are therefore a measure of the lifetime of the disturbance pattern as it is swept along with the mean flow. The variation of the longitudinal correlation coefficient of the total fluctuation field measured at optimum time delay is shown in figure 8. The optimum correlation decreases as the space separation increases. This decrease as a function of wire separation is more pronounced close to the wall, which shows that the lifetime of the disturbances is smaller where the local shear is greater. In the case of the filtered turbulent field the influence of frequency combines with the influence of separation distance and y/δ (see figure 9). When these distances are fixed, the higher the frequency the more the optimum correlation coefficient decreases. This indicates that the smaller scale disturbances are decaying at a faster rate than the larger ones. It also explains the selective part played by the longitudinal separation, which reduces the contribution of the small-scale fluctuations to the correlation coefficient of the total turbulent field as the wire separation increases.

A test of Taylor's hypothesis (Taylor 1938) that turbulence may be regarded as

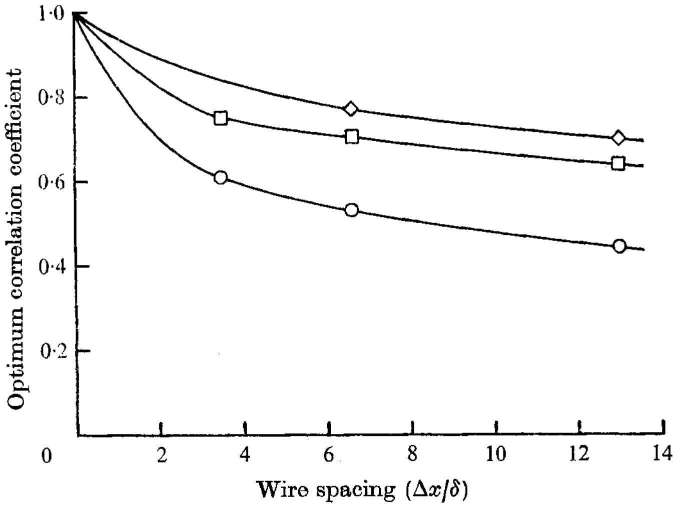

FIGURE 8. Variation of the optimum space–time correlation measurements of the total turbulent field versus the longitudinal wire separation distance Δx at three positions across the boundary layer. ○, $y/\delta = 0{\cdot}08$; □, $y/\delta = 0{\cdot}15$; ◇, $y/\delta = 0{\cdot}30$.

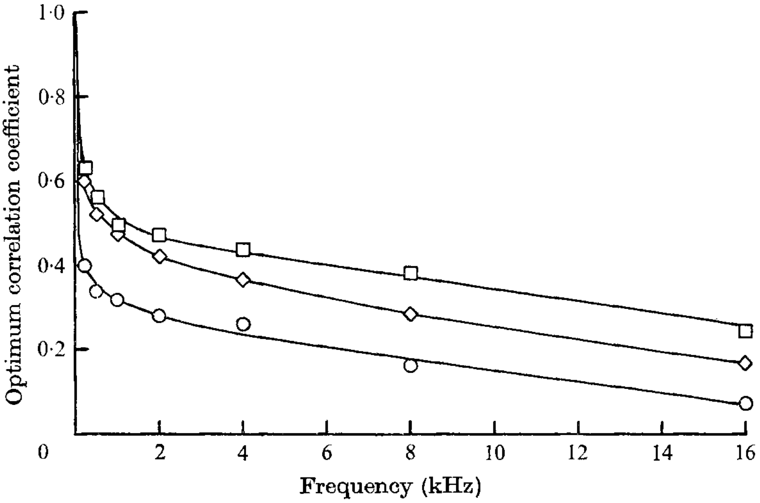

FIGURE 9. Variation of the optimum space–time correlation measurements of the filtered turbulent field versus frequency at three positions across the boundary layer for a constant longitudinal wire separation of $\Delta x/\delta = 12{\cdot}8$. ○, $y/\delta = 0{\cdot}08$; ◇, $y/\delta = 0{\cdot}3$; □, $y/\delta = 0{\cdot}6$.

a frozen pattern of eddies being swept past the wire is shown in figure 10 for three positions across the boundary layer. The longitudinal space correlations and the autocorrelation measured midway between the two wires are compared. This comparison shows that near the wall where the shear is high Taylor's hypothesis is far from satisfied. However, further from the wall ($y/\delta \gtrsim 0{\cdot}15$) the agreement between the auto- and space-correlations is much improved. Since the agreement between the auto- and space-correlations also improves as $\Delta x/U_c$ increases, i.e. when the contribution of the large-scale fluctuations to the correlation coefficient

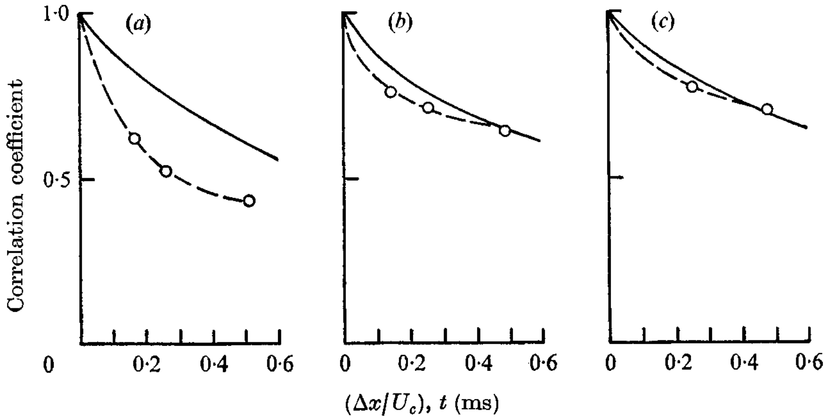

FIGURE 10. Comparison of auto- and space-correlation measurements at three positions across the boundary layer. —, autocorrelation; - - -, space correlation. (*a*) $y/\delta = 0{\cdot}08$. (*b*) $y/\delta = 0{\cdot}15$. (*c*) $y/\delta = 0{\cdot}03$.

		Frequency (kHz)							
y/δ	$\Delta x/\delta$	All	0·2	0·5	1	2	4	8	16
0·08	3·5	0·64	—	—	0·60	0·60	0·62	0·64	0·66
	6·6	0·72	—	—	0·71	0·71	0·72	0·74	0·75
	12·8	0·74	0·74	0·74	0·74	0·75	0·75	0·75	0·75
0·16	3·5	0·68	—	—	0·64	0·64	0·66	0·68	0·68
	6·6	0·79	—	—	0·76	0·76	0·78	0·79	0·79
	12·8	0·78	0·76	0·78	0·79	0·79	0·79	0·79	0·79
0·33	1·0	—	—	—	0·73	0·73	0·77	0·79	0·79
	3·5	—	—	—	0·72	0·74	0·77	0·77	0·78
	6·6	0·75	—	—	0·78	0·80	0·82	0·86	0·88
	12·8	0·82	0·80	0·82	0·82	0·83	0·83	0·86	0·87
0·65	3·5	0·78	—	—	0·67	0·79	0·84	0·86	0·89
	6·6	0·75	—	—	0·75	0·81	0·84	0·86	0·89
	12·8	0·82	0·77	0·80	0·82	0·84	0·87	0·89	0·92

TABLE 3. Ratio of the disturbance convection velocity to the boundary-layer edge velocity (U_c/U_e) for various frequency ranges through the boundary layer.

of the total turbulent field is more dominant, it is again apparent that the large-scale fluctuations decay at a slower rate than the high frequency (small-scale) fluctuations.

4.2. *Convection velocity measurements*

The results of a series of filtered (4kHz) cross-correlation measurements at several positions across the boundary layer are shown in figure 11. It can be seen that each cross-correlation curve reaches a maximum at a non-zero value of the time delay, clearly indicating the presence of convection. The amplitude of this maximum is a function of the wire separation distance Δx. A convection velocity of these disturbances may be determined from the time delay at which the maximum of a particular cross-correlation occurs.

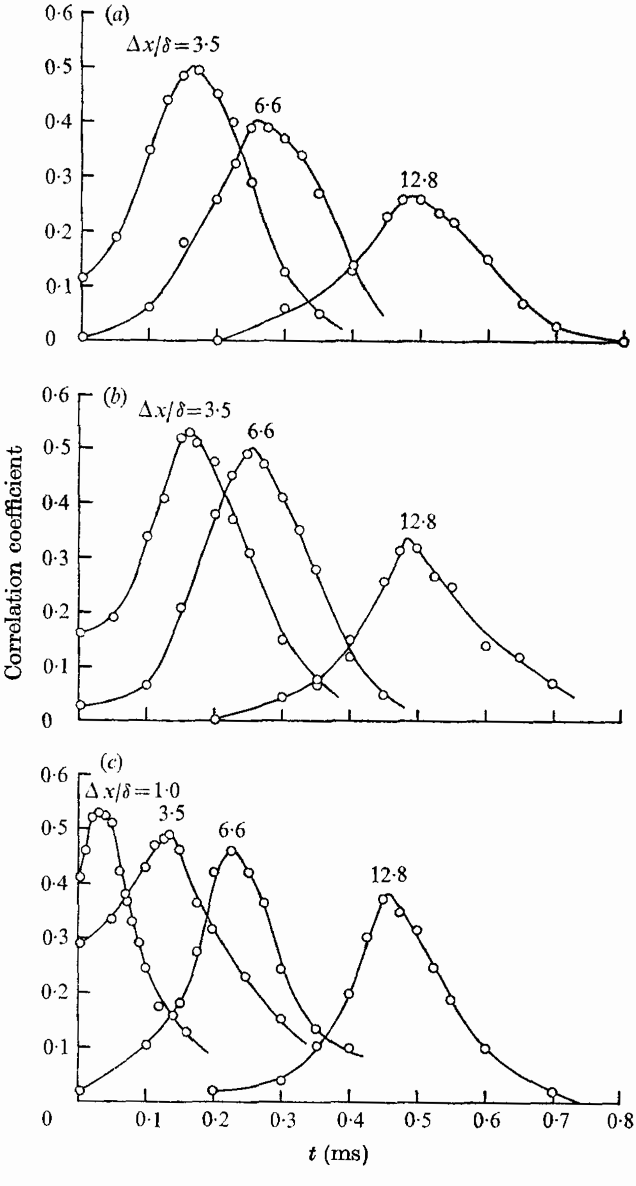

FIGURE 11. Examples of the filtered space–time correlation coefficients (4 kHz) obtained for various longitudinal wire separations $\Delta x/\delta$ at three positions across the boundary layer. (*a*) $y/\delta = 0{\cdot}08$. (*b*) $y/\delta = 0{\cdot}16$. (*c*) $y/\delta = 0{\cdot}33$.

These convection velocities, normalized by the velocity at the edge of the boundary layer, are shown as a function of wire spacing in figure 12. The data obtained over the entire frequency range of the experiment are tabulated in table 3. The variation of the disturbance convection velocity with wire separation is very pronounced close to the wall. The variation of the disturbance convection velocity relative to the local velocity within the boundary layer as a function of disturbance scale is shown for one wire spacing in figure 13. The ratio of the

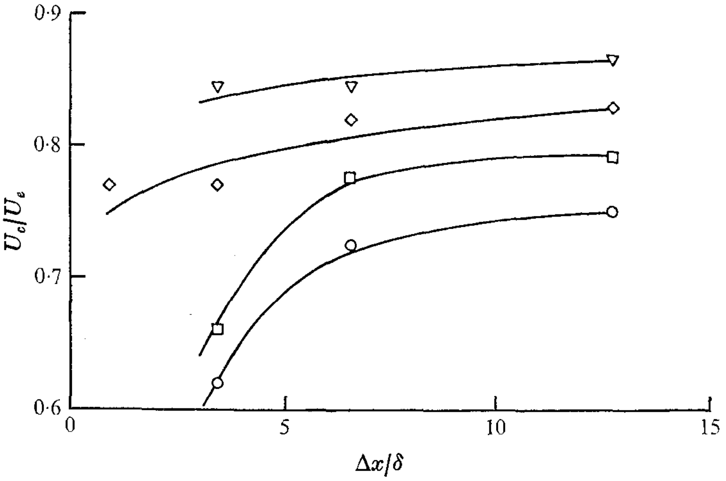

FIGURE 12. Variation of the ratio of measured disturbance convection velocity to the mean flow boundary-layer edge velocity (U_c/U_e) with longitudinal wire spacing ($\Delta x/\delta$) at four positions across the boundary layer. ○, $y/\delta = 0{\cdot}08$; □, $y/\delta = 0{\cdot}16$; ◇, $y/\delta = 0{\cdot}33$; ▽, $y/\delta = 0{\cdot}65$.

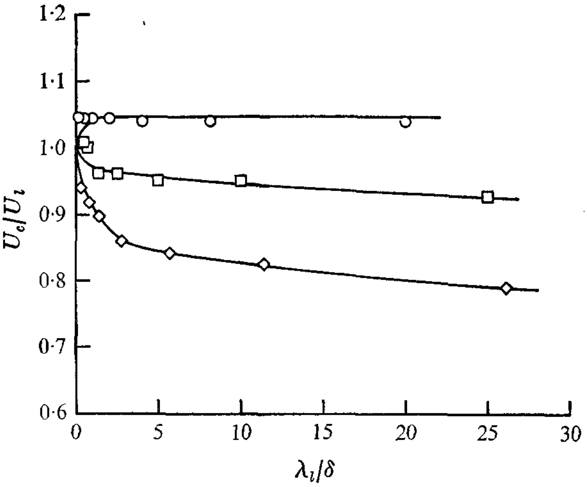

FIGURE 13. The effect of local disturbance scale $\lambda_l = U_l/2\pi f$ on the measured ratio of disturbance convection velocity to the local mean flow velocity (U_c/U_l) at three positions across the boundary layer for a constant longitudinal wire separation ($\Delta x/\delta = 12{\cdot}8$). ○, $y/\delta = 0{\cdot}08$; □, $y/\delta = 0{\cdot}33$; ◇, $y/\delta = 0{\cdot}67$.

disturbance convection velocity to the local mean velocity (U_c/U_l) tends towards unity as the scale ($\lambda_l = U_l/2\pi f$) decreases, thus the small-scale fluctuations are convected with the local mean velocity; however, as the scale increases, the more U_c/U_l differs from unity. Close to the wall ($y/\delta = 0{\cdot}08$) the propagation velocity of the large-scale disturbances is greater than the local velocity whereas it is significantly lower than the local velocity in the outer half of the boundary layer.

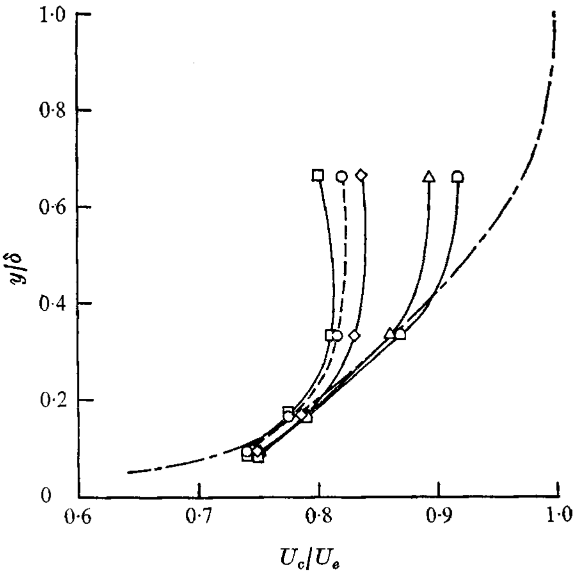

FIGURE 14. The distribution of disturbance convection velocities U_c for various disturbance scales $\lambda_e = U_e/2\pi f$ across the boundary layer and comparison with the local mean flow velocity U_l. □, $\lambda_e/\delta = 9\cdot6$; ◇, $\lambda_e/\delta = 2\cdot4$; △, $\lambda_e/\delta = 0\cdot6$; ⌂, $\lambda_e/\delta = 0\cdot3$. - - ○ - -, total; — - —, U_l/U_e.

The variation of the convection velocity profiles for the total and filtered turbulent fields are compared with the mean velocity profile in figure 14. At a distance from the wall $y/\delta \approx 0\cdot15$, the convection velocity corresponding to the various scales are equal to the local fluid velocity, i.e. $U_c \approx 0\cdot78\,U_e$, where U_e is the velocity at the edge of the boundary layer. At greater values of y/δ the differences increase with the scale; in the outer portion of the boundary layer the large-scale disturbances are convected more slowly than the mean velocity and in the inner region more rapidly than the mean velocity. In fact, the convection velocity of the large-scale disturbances varies little across the boundary layer.

The values of the cross-correlation coefficient have also been determined for various separation distances normal to the wall as a function of the time delay. Figure 15 shows the resulting filtered (3 kHz) correlation coefficients for the case where one hot wire was kept at a fixed distance from the wall ($y/\delta = 0\cdot06$) while the second wire was set at different separation distances directly above the first wire. It can be seen that the correlation reaches a maximum value for an optimum time delay t applied to the fluctuations sensed by the probe located farthest from the wall. This optimum time delay, which is a function of the normal separation distance and y/δ, has been observed previously in an incompressible turbulent boundary layer (Favre *et al.* 1967). These space–time correlations may be interpreted in terms of a disturbance inclination angle α to the wall. (Additional correlation measurements made between two wires traversed through the boundary layer with constant normal separation gave similar results.) This time-averaged angle may be determined by dividing the normal wire separation distance by the

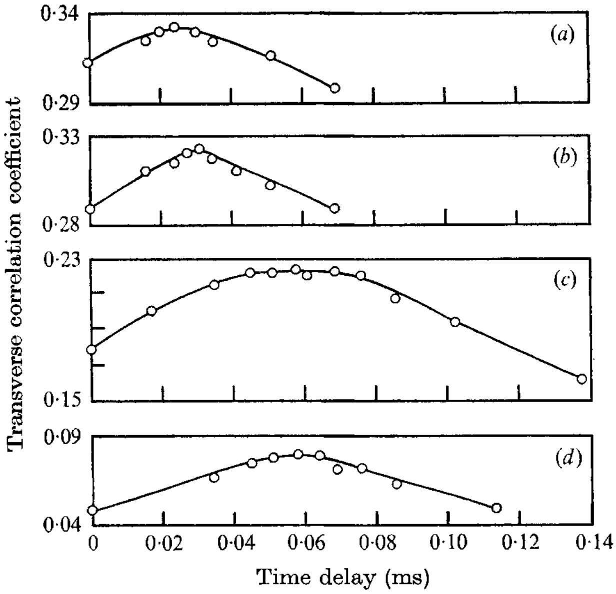

FIGURE 15. Examples of transverse space–time correlations of the filtered (3 kHz) turbulent field for four positions of the outer wire (y_2/δ) across the boundary layer. The inner wire remained at a constant position ($y_1/\delta = 0{\cdot}06$). Positive time delay represents the signal from the outer wire being delayed with respect to the inner wire. (*a*) $y_2/\delta = 0{\cdot}19$. (*b*) $y_2/\delta = 0{\cdot}39$. (*c*) $y_2/\delta = 0{\cdot}59$. (*d*) $y_2/\delta = 1{\cdot}0$.

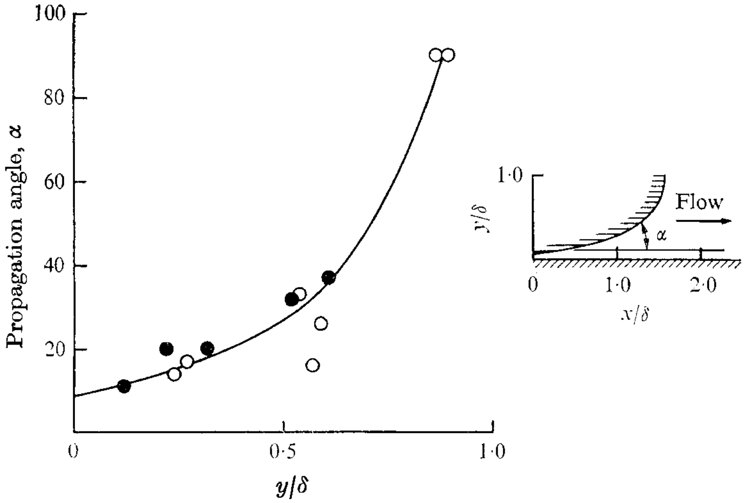

FIGURE 16. Variation of the measured disturbance inclination angles across the boundary layer. ○, 1 kHz; ●, 3 kHz.

product of the observed time delay (for the maximum correlation coefficient) and the disturbance convection velocity at the outer wire location. The results, presented in figure 16, show that the time-averaged inclination angle is smallest close to the wall and increases with increasing distance from the wall.

5. A proposed model of turbulence generation

In figure 12 it was found that, close to the wall, the measured disturbance convection velocities increased with increasing wire separation. This implies an outward dispersion of the turbulent fluctuations from the low velocity region close to the wall. This implication is supported by the data in figure 16 since, as the disturbance propagation angle increases, the variation of the convection velocity with wire separation away from the wall is greatly reduced. Indeed, when the disturbance fronts are normal to the wall no variation of convection velocity with spacing would be expected. However, it could be argued that the variation of convection velocity with distance could be the result of the spatial separation acting as a filter, which would minimize the contribution of the smaller scale fluctuations at large separation distances. Even filtering the signals does not altogether overcome the problem since the apparent disturbance frequency is a function of both scale and convection velocity. However, since it has already been shown (figures 13 and 14) that close to the wall there is little variation of convection velocity with scale, this filtering effect would not account for the measured variations. In fact, away from the wall, since the large-scale disturbances travel more slowly than the smaller scale ones a decrease in convection velocity with spacing might have been expected had this effect been dominant.

It is suggested therefore that in hypersonic turbulent boundary layers the turbulent fluctuations originate close to the wall and propagate outwards as they are convected downstream. The time-averaged trajectory of such a disturbance is shown in figure 16. The propagation angle α of between 10° and 20° measured close to the wall is in surprisingly good agreement with the incompressible experiments of Kline *et al.* (1967), in which ejected streaks were observed to leave the wall layer at an angle of about 10°–12°.

Some insight into the three-dimensional structure of these turbulent disturbances may be obtained from figure 17, where the results of the variation in the optimum lateral correlation (which occurred at zero time delay) across the boundary layer are presented. These results indicate that the disturbances are very narrow close to the wall and that they grow laterally as they propagate away from the wall. These data together with those discussed previously suggest that turbulence production in a hypersonic turbulent boundary layer is created by highly three-dimensional disturbances originating close to the wall. The form of such a disturbance, suggested by the hot-wire correlation data, is shown in figure 18.

At first sight the steep trajectories in the outer portion of the boundary layer suggest that the bursts may move across Mach lines. However, it must be borne in mind that the relative velocity between the disturbance and the local mean velocity is always subsonic so that the bursts are as free to propagate as they

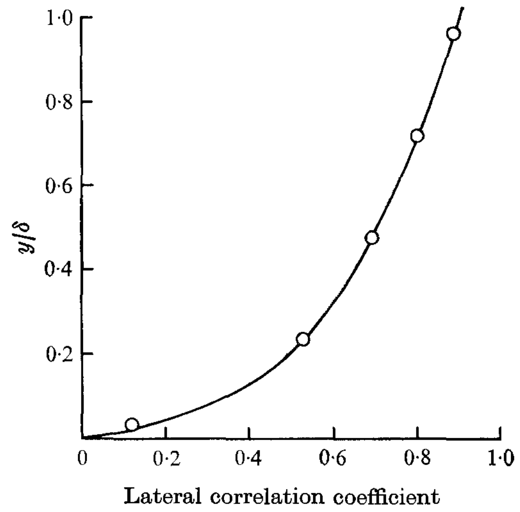

FIGURE 17. Variation of the optimum lateral correlation measurements across the boundary layer for a lateral wire separation $\Delta z/\delta = 0{\cdot}77$.

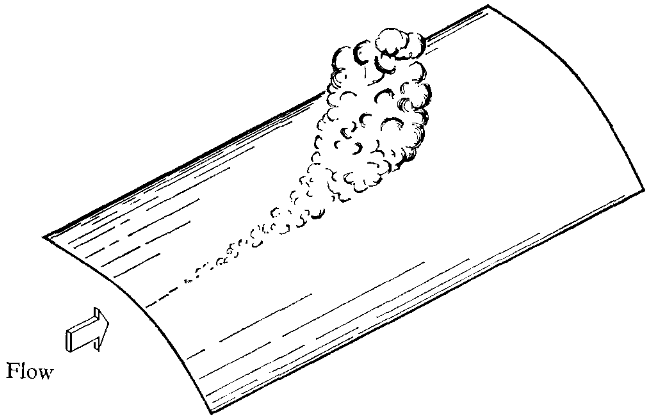

FIGURE 18. Proposed model of turbulence generation.

would be in an incompressible flow. Although the idea of a burst lifetime should not be taken too literally, the space–time correlation measurements show that the larger eddies persist for downstream distances of the order of 50 boundary-layer thicknesses.

The structure of any turbulent flow is the result of the local balance of production, dissipation and transport of the turbulent kinetic energy. In particular, since the structure of a hypersonic turbulent boundary layer is maintained by the production of turbulent kinetic energy, some knowledge of this rate of production is valuable.

Previous work on incompressible flows has accumulated evidence that the turbulence production process is composed of a sequence of events having a

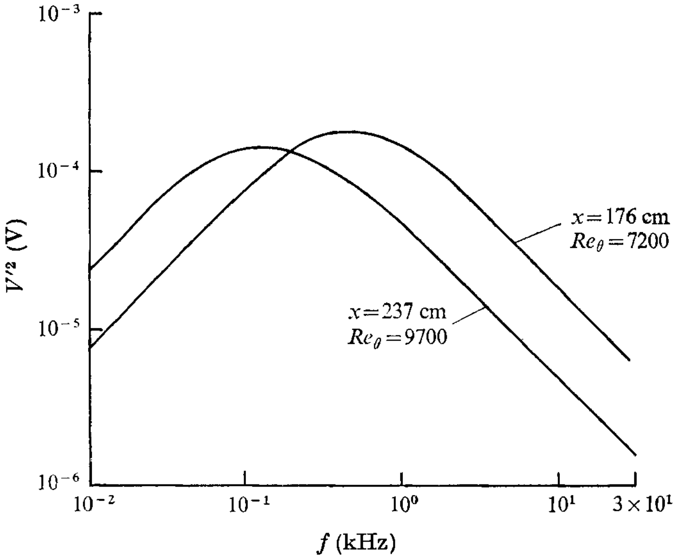

FIGURE 19. Power spectra in viscous sublayer (y/δ = 0·01) at two stations on the model.

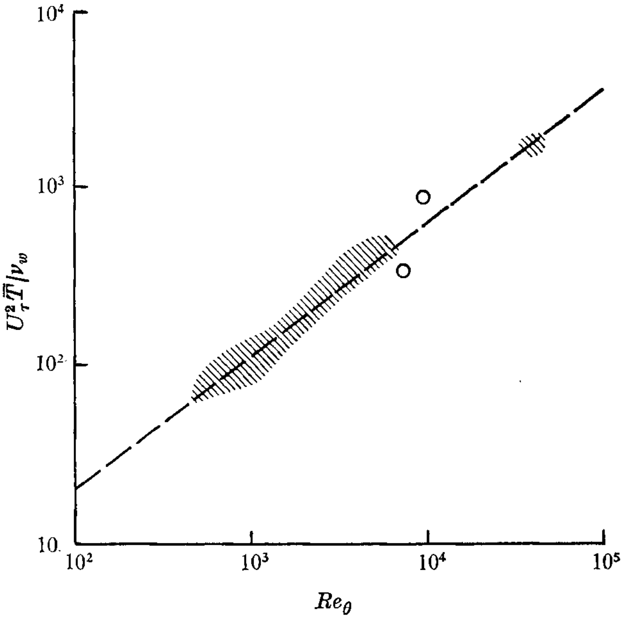

FIGURE 20. Momentum Reynolds number dependence of the time interval between bursts ($\bar{T}$) normalized by inner variables. ○, present data; ▨, previous incompressible data.

probabilistic overall time period between bursts. These data have been collected by Laufer & Badri Narayanan (1971) and correlated using inner variables and Re_θ. In the present case, the time interval between bursts has been estimated from the energy peaks in the hot-wire power spectra obtained in the viscous sublayer.† These spectra are shown in figure 19, where it can be seen that the maximum fluctuation energy at the two streamwise locations occurs at 140 and 400 Hz. If we assume that these frequencies are representative of the dominant time interval between bursts, the corresponding times can be calculated ($\overline{T} = \frac{1}{2}\pi f$), and are compared with previous incompressible data in figure 20. It can be seen that the present data obtained at hypersonic speeds are in excellent agreement with those obtained in incompressible flows. However, the estimated time intervals between bursts do not correlate when scaled using outer variables (Kim *et al.* 1971). This might be expected since the relationship between inner and outer variables is altered in compressible boundary layers.

Thus the present hot-wire data suggest a picture of turbulent production in hypersonic boundary layers which is consistent with previous results obtained in incompressible flows.

The authors wish to thank M.I. Kussoy, who was responsible for the skin-friction measurements. This research was conducted while one author (F.K.O.) held a National Academy of Sciences – National Research Council Postdoctoral Resident Research Associateship supported by the National Aeronautics and Space Administration.

Appendix. Mean boundary-layer measurements

The surface pressure, skin friction and heat transfer were obtained along the cylindrical portion of the model from $x = 85$ to 237 cm. The skin friction was measured directly using a contoured floating-element balance. Direct calibrations using weights hung from the sensing element were performed before and after each test series. These calibrations were repeatable to within 5 %. The heat-transfer rate was measured using the thin-wall transient technique. Lateral and radial conduction errors were computed and found to be less than 5 % of the convective heat transfer. To compute the Stanton number the adiabatic wall temperature was assumed to be 0·9 of the total temperature. The accuracy of the skin-friction and heat-transfer measurements was calculated to be ± 8 %.

With the assumption that the static pressure is constant through the boundary layer, only Pitot pressure and total temperature surveys are needed to calculate velocity, Mach number and density profiles. Such profiles were obtained at $x = 115$, 176 and 237 cm.

To provide reliable mean flow profiles extra care was taken to use flow field instrumentation which required little or no experimental corrections. Single probes were traversed through the boundary layer, stopping every few seconds to ensure no time lag in pressure or temperature. Pitot pressure was measured

---

† It has been shown previously (Owen 1970) that the total hot-wire voltage fluctuation V' may be written as $V' = f(\gamma V'_T, nV'_{LT})$, where γ is the intermittency factor, n the burst frequency, V'_T the voltage fluctuation due to turbulent flow associated with spot passage and V'_{LT} the voltage fluctuation caused by changes in mean voltage across the wire from the laminar to the turbulent levels. Since $V'_{LT} \gg V'_T$ the peak in the power spectra of V' should occur at a frequency which is representative of the dominant time interval between bursts.

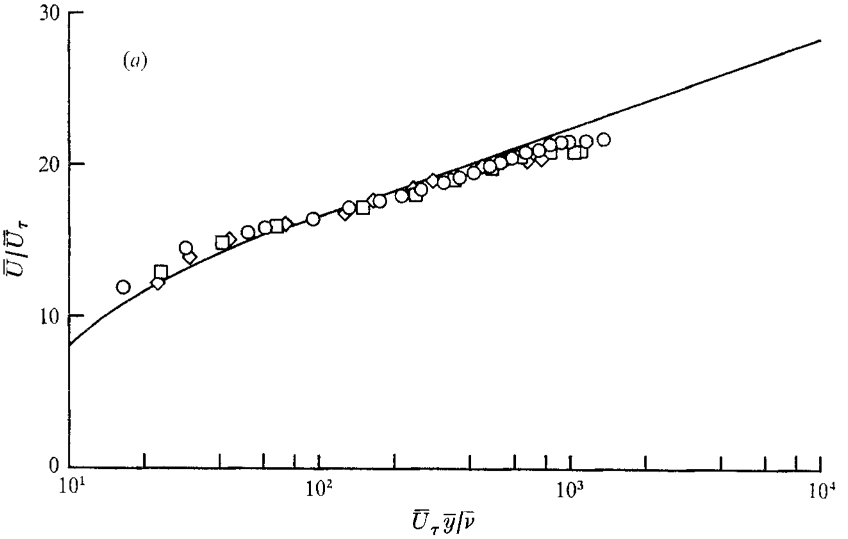

FIGURE 21 (*a*). For legend see page 630.

with a rectangular stainless steel probe (with outside dimensions 0·075 cm high by 0·19 cm wide with a uniform wall thickness of 0·005 cm). Independent calibrations in a free-jet facility, matching Mach number, velocity and density with the present test conditions, indicated that rarefaction effects were less than 0·5 %. The minimum local probe Reynolds number based on conditions behind the normal shock and probe height was 60. The Pitot probe height was less than 4·5 % of the smallest boundary-layer thickness traversed.

Total temperature profiles were obtained using two types of probes; a single shielded chromel–alumel probe 0·14 cm in diameter was used in the outer 90 % of the boundary layer and an unshielded butt-welded chromel–alumel wire 0·3 cm long by 0·007 cm thick was used close to the wall. Independent calibrations of these probes in a free-jet facility, matching test conditions, indicated a maximum total temperature error of 2 % for the shielded probe and 5 % for the unshielded probe. Corrections were only applied to the unshielded probe. For portions of the boundary layer where measurements with both probes were taken the corrected data agreed to within 2 %. The shielded probe diameter was less than 8 % of the smallest boundary-layer thickness traversed.

The calculated probable errors for the measured and calculated flow field quantities are ± 3 % for the total temperature, Mach number and velocity and 5 % for the density.

Two important methods used to predict compressible turbulent boundary-layer flow fields are compressible–incompressible transformation techniques and the finite-difference solutions of the full time-averaged partial differential boundary-layer equations. The appeal of the transformation techniques is the desire to employ their simplicity and accuracy for simple flat-plate flows, whereas the virtue of the finite-difference solutions is that they can be extended to more complex flows such as those with a pressure gradient. However, the latter tech-

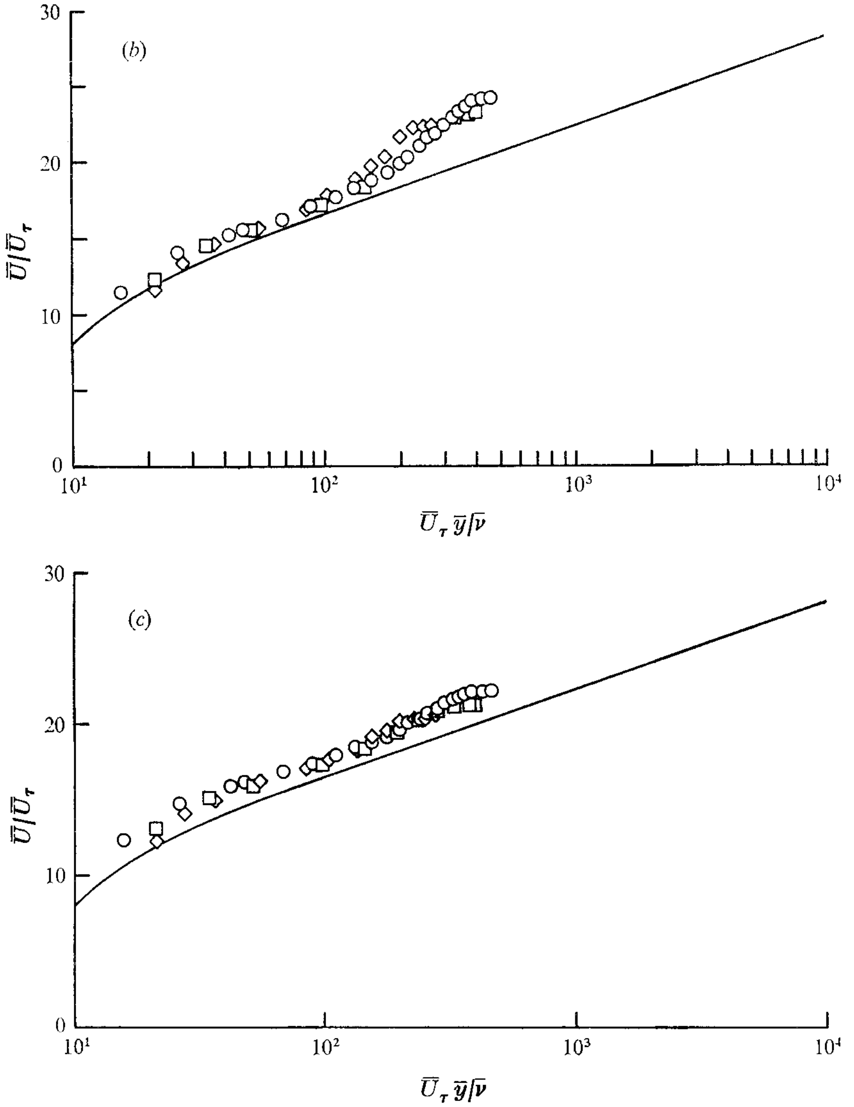

FIGURE 21. Law-of-the-wall correlation in incompressible co-ordinates. —, incompressible case, Coles (1953). ○, x = 237 cm; □, x = 176 cm; ◇, x = 115 cm. (*a*) Using the Baronti & Libby transformation. (*b*) Using the Van Driest transformation. (*c*) Using the wall reference temperature transformation.

nique involves a significant amount of empiricism regarding the model for Reynolds-stress terms and the turbulent Prandtl number.

Three representative transformation techniques have been applied to the present data. They are the methods of Baronti & Libby (1966), Van Driest (1956) and the wall reference temperature technique. The transformation equations for these techniques are listed by Hopkins *et al.* (1972). The three velocity profiles (shown in figure 3) are transformed to law-of-the-wall variables by each of the three techniques in figures 21(*a*), (*b*) and (*c*). A comparison with

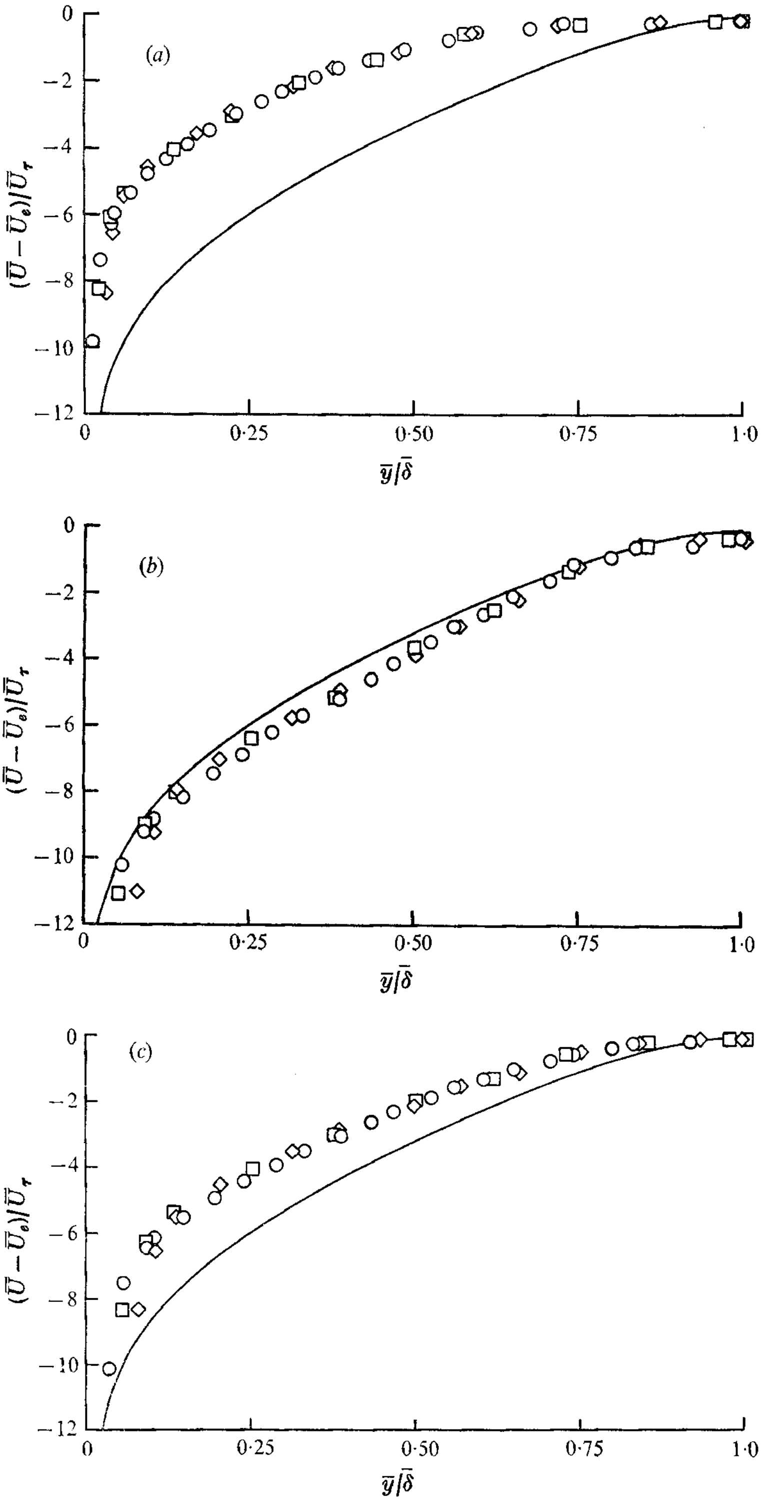

FIGURE 22. Velocity-defect profiles in incompressible co-ordinates. —, incompressible case, Coles (1953). ○, $x = 237$ cm; □, $x = 176$ cm; ◇, $x = 115$ cm. (*a*) Using the Baronti & Libby transformation. (*b*) Using the Van Driest transformation. (*c*) Using the wall reference temperature transformation.

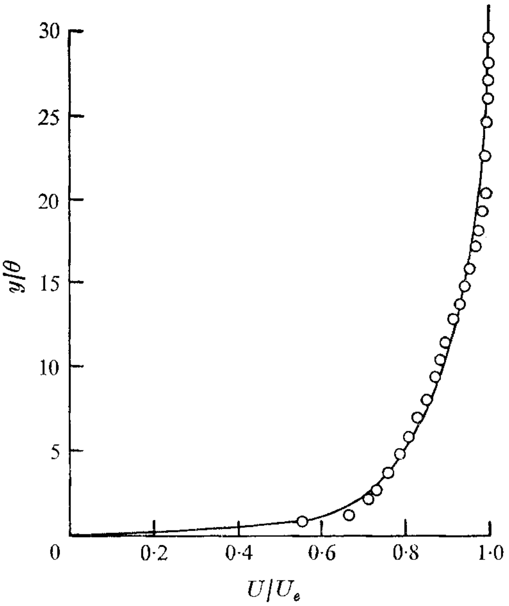

FIGURE 23. Comparison of the mean velocity profile (points) with finite-difference predictions (solid line) at the $x = 237$ cm location.

the incompressible curve of Coles (1953) indicates the adequacy of each transformation for the law-of-the-wall portion of the boundary layer. For these transformations the boundary-layer thickness δ was redefined as the thickness determined by extrapolation of the measured velocity profile in the power-law form $\ln U/U_e$ *vs.* $\ln y$ to $U/U_e = 1{\cdot}0$. For each case this thickness was approximately equal to 87 % of the Pitot pressure boundary-layer thickness. The wall friction velocity used is tabulated in table 2 and was calculated using the direct skin-friction measurements. For $x = 115$ cm an interpolated value of wall friction velocity was used. The method of Baronti & Libby has the correct magnitude but a slight difference in slope between the transformed data and the incompressible transformation. Near the wall, Van Driest's method has the correct slope and shows a wake-like region near the outer edge of the boundary layer similar to incompressible flows, e.g. Coles (1953). The wake region is not obtained using Baronti & Libby's method. A less distinct wake-like region is observed for the wall reference temperature method. No significant variation with x is noted for any of the transformations. The agreement with Baronti & Libby's method is in accord with previous hypersonic work, e.g. Bertram *et al.* (1968). This agreement also verifies the method for obtaining wall skin friction from turbulent velocity profiles in a hypersonic zero-pressure-gradient flow. This method predicts the present measured skin-friction data to an accuracy of ± 10 %.

These velocity profiles are also transformed to velocity-defect variables by each technique in figures 22(*a*), (*b*) and (*c*). The solid line in each figure is the incompressible correlation of Coles (1953). Note the apparent failure of the Baronti & Libby method and the success of the Van Driest method in the outer portion of

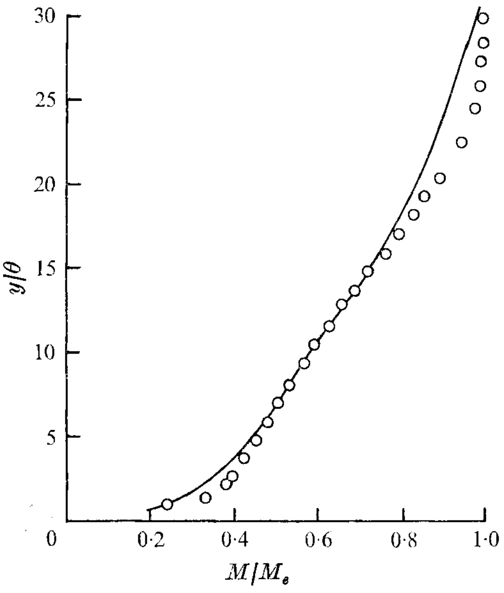

FIGURE 24. Comparison of the mean Mach number profile (points) with finite-difference predictions (solid line) at the $x = 237$ cm location.

the boundary layer. The Van Driest agreement is consistent with the wake-like behaviour displayed with the 'law-of-the-wall' variables (figure 21 (*b*)). A similar failure for hypersonic flow was also noted by Baronti & Libby in their original analysis. The present data do not offer any additional information to explain this failure but in fact verify that a compressible zero-pressure-gradient flow transforms to a favourable-pressure-gradient incompressible flow as first suggested by Baronti & Libby (1966). It is concluded that the Van Driest transformation is superior for both law-of-the-wall and defect profiles.

The data are also compared with the finite-difference program of Dwyer (see Hopkins *et al.* 1972). The calculation was started with a fully turbulent boundary layer at the midpoint of the measured transition region. The turbulent Prandtl number was assumed to be 0·9. The solutions are compared with the data obtained at the last survey station ($x = 237$ cm) in figures 23, 24 and 25. There is reasonable agreement between theory and experiment over the entire boundary layer, except for the Mach number and density profiles near the wall and at the outer edge. Similar comparisons were obtained at the two forward survey stations.

The experimental temperature–velocity relationships for the present tests are shown in figure 26. Note that the data are identical for all three survey stations. Also shown are the linear (Crocco), quadratic and finite-difference solution relationships. The data fall midway between the linear and quadratic relationships.

It is interesting to note that although the last survey station is over 80 average boundary-layer thicknesses downstream from the cone–cylinder expansion there is no indication of a relaxation of the data towards a linear relationship. It has been argued by Bushnell *et al.* (1969) that a hypersonic turbulent boundary layer

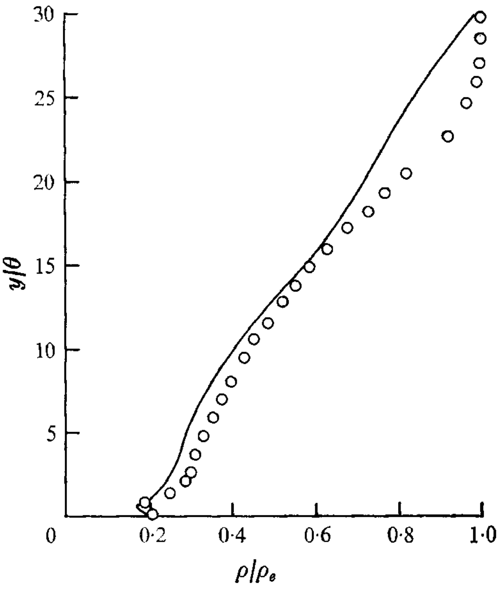

FIGURE 25. Comparison of the mean density profile (points) with finite-difference predictions (solid line) at the $x = 237$ cm location.

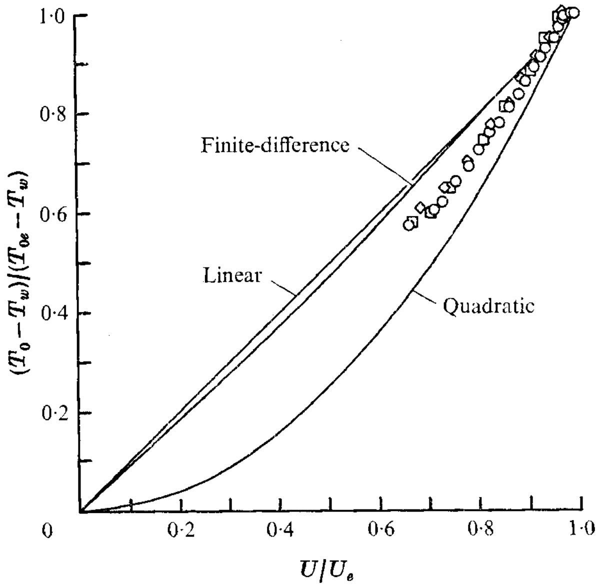

FIGURE 26. Velocity–total-temperature distribution across the turbulent boundary layer. ○, $x = 237$ cm; □, $x = 176$ cm; ◇, $x = 115$ cm.

will relax towards a linear relationship far downstream from a pressure gradient region. The present results do not confirm this.

The skin-friction and heat-transfer results are presented in figures 27 and 28. To remove any uncertainty concerning the appropriate origin of turbulent flow on the model the data are plotted as a function of the momentum thickness

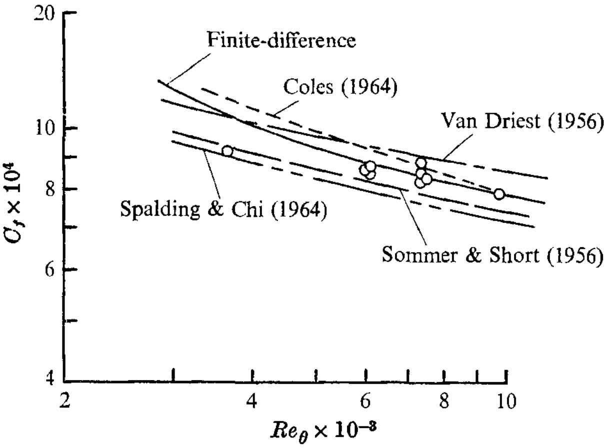

FIGURE 27. Measured local skin-friction distribution and comparison with several prediction methods.

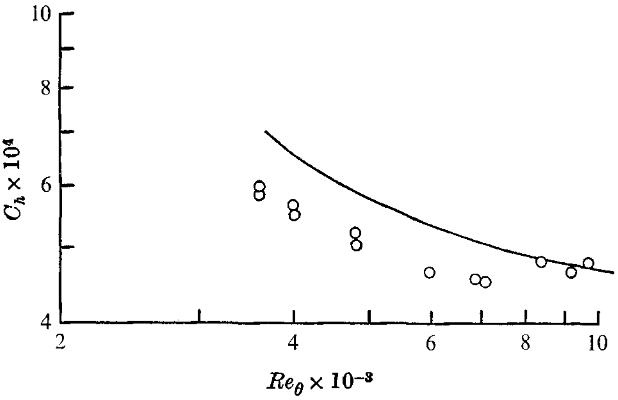

FIGURE 28. Measured local Stanton number distribution (points) and comparison with finite-difference predictions (solid line).

Reynolds number based on boundary-layer edge quantities. In figure 27 the measured skin friction is compared with five prediction methods. With four of these methods, the Kármán–Schoenherr equation is used with the appropriate transformations to relate the incompressible $\overline{C_f}(\overline{Re_\theta})$ to the compressible $C_f(Re_\theta)$. This is discussed in detail by Hopkins *et al.* (1972). The five most commonly used prediction methods bracket the data. In figure 28 the measured heat-transfer results are shown. The data are only compared with the finite-difference predictions, since the other methods shown in figure 27 predict Stanton number only if a Reynolds analogy factor is assumed. The finite-difference solution over-predicts the data from 0 to 15 %.

The Reynolds analogy factors $2C_h/C_f$ computed from these data vary from 1·26 to 1·07 (see table 2). Since the end of transition is at $x = 80$ cm the first analogy factor ($x = 85$ cm) may not be representative of a fully developed turbulent boundary layer.

REFERENCES

Baronti, P. O. & Libby, P. A. 1966 *A.I.A.A. J.* **4**, 193.

Bertram, M. H., Cary, A. M. & Whitehead, A. H. 1968 *AGARDograph*, no. 30.

Bushnell, D. M., Johnson, C. B., Harvey, W. D. & Feller, E. V. 1969 *N.A.S.A. Tech. Note*, D-5433.

Coles, D. 1953 *Jet Propulsion Lab., California Institute of Technology Rep.* no. 20–69.

Coles, D. 1964 *Phys. Fluids*, **7**, 1403.

Favre, A., Gaviglio, J. & Dumas, R. 1967 *Phys. Fluids*, **10** (suppl.), 138.

Hopkins, E. J., Keener, E. R., Polek, T. E. & Dwyer, H. A. 1972 *A.I.A.A. J.* **10**, 40.

Kim, H. T., Kline, S. J. & Reynolds, W. C. 1971 *J. Fluid Mech.* **50**, 133.

Kline, S. J., Reynolds, W. C., Schraub, F. A. & Runstadler, P. W. 1967 *J. Fluid Mech.* **30**, 741.

Laufer, J. 1968 *N.A.S.A. Special Publ.* no. 216.

Laufer, J. & Badri Narayanan, M. A. 1971 *Phys. Fluids*, **14**, 182.

Owen, F. K. 1970 *A.I.A.A. J.* **8**, 518.

Sommer, S. C. & Short, B. J. 1956 *J. Aero. Sci.* **23**, 536.

Spalding, D. B. & Chi, S. W. 1964 *J. Fluid Mech.* **18**, 117.

Taylor, G. I. 1938 *Proc. Roy. Soc.* A **164**, 476.

Van Driest, E. R. 1956 *Aero Aspects Session, National Summer Meeting, IAS, Los Angeles.*